Air–Sea Interaction during an Extreme Cold Air Outbreak from the Eastern Coast of the United States

ROBERT L. GROSSMAN

Cooperative Institute for Research in the Environmental Sciences, University of Colorado/NOAA, Boulder, Colorado

ALAN K. BETTS

Middlebury, Vermont

(Manuscript received 7 April 1989, in final form 8 September 1989)

ABSTRACT

The area east of the coast of North Carolina chosen for enhanced observation during the Genesis of Atlantic Lows Experiment (GALE) has one of the highest average wintertime energy transfers from ocean to atmosphere on earth. A substantial part of this transfer occurs in the aftermath of winter storms as cold, dry air flows off of the continent over the warm Gulf Stream. We report on an aircraft investigation of boundary layer mean and turbulent structure and evaluate the Lagrangian budgets of temperature and moisture in the subcloud layer following a streamline during an extreme cold air outbreak. The maximum sea–air temperature difference was 23 K. Two aircraft were used: the NCAR Electra, which measured turbulent fluxes and investigated subcloud layer conditions, while the NASA Electra, using a lidar, measured the height of cloud tops. A stratocumulus overcast was found from about 60 km offshore to the Gulf Stream core with cloud top rising downstream. East of the Gulf Stream cumulus congestus and snow showers were observed. Cloud base decreased downstream and numerous steam plumes filled the subcloud layer. Temperatures were corrected for the substantial effects of diurnal variation in order to isolate air–sea interaction processes. Cross sections show most warming, and moistening of the subcloud layer occurred before the Gulf Stream core. Windspeeds increased downstream and maxima were observed near cloud top (inversion) and in the subcloud layer. Lagrangian budgets showed most warming, and moistening of the layer between 70 m and about 100 m below mean cloud base was due to turbulent flux divergence. At 70 m a maximum total heat flux of 1174 W m^{-2} (364 W m^{-2} sensible, 799 W m^{-2} latent) was observed over the Gulf Stream core. In the temperature budget, the radiative flux divergence term was relatively small and a residual condensation warming was inferred. Complementary drying was estimated from the residual of the moisture budget. The budgets were combined using a graphical technique on a conserved parameter ($\theta - q$) diagram and were extrapolated into the surface layer with reasonable results. This technique was also applied to the entire subcloud layer with results that implied that east of the Gulf Stream entrainment fluxes at cloud base and evaporation of falling precipitation may act to cool and dry the subcloud layer, reducing the effects of flux convergence (which would warm and moisten). The Lagrangian warming and moistening rates we estimated indicate that cold, dry continental air can be transformed to air which can participate in deep convection (which appears to be an integral part of rapid cyclogenesis) in about 20–30 hours.

1. Introduction

In analyzing estimates of the global energy budget during the Northern Hemisphere winter Palmen and Newton (1966) show that radiative losses in the atmosphere are balanced by heat given up by storage from the oceans. They estimate that about 70% of the total change in oceanic heat storage occurs in winter resulting in an estimated mean cooling of the upper 200 m of the ocean by 0.86°C. Studies cited by them point out that the greatest changes in ocean heat storage occur in the latitude belt 30 to 40 degrees where the estimated heat loss of 70 W m^{-2} is almost double that of the summer maximum (which occurs in the 20–30 degree belt). This latitude belt, especially in the Northern Hemisphere, is a zone in which there is a maximum of winter synoptic disturbances (viz. Long and Hanson 1985) that would enhance air–sea energy exchange. Using ship reports applied to the bulk aerodynamic formulae for estimating near surface sensible and latent heat fluxes, Budyko (1963) showed that the most intense energy exchange from ocean to atmosphere takes place off the coasts of Japan and the United States.

The chief reason for the enhancement of energy exchange from ocean to atmosphere off of the eastern Japanese and North American coasts is the presence of oceanic western boundary currents, respectively the Kuroshio and Gulf Stream systems. Here the sea–air temperature differences as well as sea–air moisture gradients are maximum and are associated with rela-

Corresponding author address: Dr. Robert L. Grossman, CIRES, University of Colorado, Campus Box 216, Boulder, CO 80309.

tively high surface wind speeds caused by large-scale pressure gradients (continental ridge, oceanic low) and lower frictional retardation due to the decrease in surface roughness from land to open sea. This is certainly the situation off the East Coast of the United States during a continental cold air outbreak when cold, dry air from the arctic zone flows offshore over the warm Gulf Stream.

Bunker and Worthington (1976) updated Budyko's annual average estimates for the North Atlantic and showed a maximum total energy loss from ocean to atmosphere of about 380 W m^{-2} (88 W m^{-2} sensible heat, 292 W m^{-2} latent heat) centered on a line between 40 N, 56 E and 35 N, 72 E. They note that this area is associated with wintertime cold, dry air flowing over the warm water of the Gulf Stream. Bunker (1976) extended this work and showed monthly average estimates of sensible and latent heat flux for selected areas over the North Atlantic. For one area near the area of maximum annual heat loss noted above, Bunker showed that total heat loss for January was 550 W m^{-2} (150 W m^{-2} sensible heat, 400 W m^{-2} latent heat). Thus, in addition to being a preferred region of rapid cyclogenesis, the area off of the East Coast chosen for the Genesis of Atlantic Lows Experiment (GALE; Mercer and Krietzberg 1986; Dirks et al. 1988) is an area of large heat losses from ocean to atmosphere. A substantial portion of this heat loss can be associated with cold air outbreaks from the continent flowing over the warm water of the Gulf Stream. Estimates of sensible heat loss from ocean to atmosphere over the Kuroshio Current during the GARP Airmass Transformation Experiment (AMTEX) show that the exchange almost doubles during cold air outbreaks (WMO 1981). Ninomiya (1973) and Ninomiya and Akiyama (1976) extensively studied moderate cold air outbreaks near Japan by using AMTEX data applied to regional scale budgets of heat and moisture. In the former study it was found that most of the heating of the atmosphere occurred below the inversion. Exploration of air–sea interaction and boundary layer accumulation of heat and moisture associated with an extreme cold air outbreak is the primary motivation for this work.

East Coast cold air outbreaks, which last from one to two days, occur about 15–20 times per winter season (Bosart, personal communication). About five of those are classed as intense, where the air temperature is at or below 0°C while Gulf Stream surface temperature is about 20°C [see also Konrad and Colucci (1989) for detailed statistics]. This investigation uses aircraft data to explore airmass transformation during an intense cold air outbreak that followed a rapid, offshore cyclogenesis on 27 January 1986.

2. Experimental design, mission plan, and data acquisition

The National Center for Atmospheric Research (NCAR) Electra research aircraft mission over the Gulf Stream near Wilmington, North Carolina on 28 January 1986 was part of the GALE. While other aircraft investigations of airmass transformation have been carried out (WMO 1981; Chou et al. 1986), this was the first for such an intense case and where the mission goal and design was to evaluate subcloud layer budgets of heat, moisture, and momentum along a streamline (Riehl et al. 1951; Grossman and Durran 1984).

We have two objectives in this work. First, we will describe the mean and turbulent structure of the subcloud layer along a streamline which was characterized by cold air flowing off shore over the Gulf Stream. Second, we will evaluate the Lagrangian budgets of heat and moisture along that streamline using two different approaches: one which uses standard techniques where the budgets are evaluated separately and a more recent graphical technique (Betts 1984) in which the budgets are combined on a conserved parameter diagram.

Bane and Osgood (1989) discuss the oceanic response to the 28 January 1986 cold air outbreak. Chou and Zimmerman (1989), using a conditional sampling technique, investigated the nature of the buoyancy flux measured by both the NCAR Electra and King Air during the same cold air outbreak.

a. Experimental design: Streamline budgets

The approximate Lagrangian budget equation for the scalar, Φ, is

$$\delta\Phi/\delta t + \partial\overline{w'\Phi'}/\partial z \approx \sum (S_o - S_i). \qquad (1)$$

The two terms on the LHS are, respectively, the time rate of change of a parcel of air as it moves with the flow and the vertical turbulent flux divergence of Φ. The overbar is the time average used to obtain the flux. The term on the RHS accounts for the sum of the sources and sinks of Φ. For our study Φ was potential temperature (θ) and moisture (ρ_v, absolute humidity or, q, specific humidity). Equation (2) explains the primes. Sources and sinks are discussed in sections 6 and 7. This equation was evaluated for a slab whose thickness was between the lowest and highest levels flown by the aircraft at each stack (a substantial portion of the subcloud layer),[1] width (cross stream) the length of an aircraft leg (approximately 35 km; see section 2b), and unit depth (along stream).

Since we wished to isolate the effects of air–sea interaction, we took great care to remove the influence of the land diurnal heating on the first term on the LHS (section 6a). The aircraft-mission plan design (Fig. 1) for 28 January serves to evaluate (1) when volumetrically integrated as described above.

[1] Because of concern about instrument wetting by cloud, the highest level flown was about 100 m below the level of cloud material viewed from the flight deck. Since cloud bases were very ragged, the mean cloud base (determined by the LCL) was probably higher (see Table 1).

In the streamline budget study by Riehl et al. (1951), which used fixed-position-ship aerological data, the important vertical flux divergence term had to be parameterized using mean values. Aircraft can fly along a streamline and with proper instrumentation measure the flux divergence directly. For this mission the flux divergence term was estimated from data obtained by flying a stack of level legs at three to four different altitudes (depending upon the height of cloud base) over a position fixed to the earth by the aircraft inertial navigation system. Normally stacks are flown crosswind to increase confidence in flux estimates (Bean et al. 1972; Grossman 1982) but the extreme sea surface temperature gradients in the vicinity of the Gulf Stream caused those GALE scientists who wished to measure turbulent fluxes from aircraft to fly parallel to sea surface isotherms. The length of these level legs, which is proportional to the statistical confidence placed on the estimated fluxes, was adjusted according to the wind direction; the shortest legs could be flown during conditions when the wind direction was perpendicular to the sea surface isotherms. During most cold air outbreaks the offshore winds are from the west–northwest so streamlines are nearly perpendicular to the sea surface temperature isotherms of the Gulf Stream; this was the case for 28 January (Fig. 1).

The Electra flux stack legs were 5–6 minutes long; about 30–36 km at Electra airspeed. Lacking evidence to the contrary, and with our limited measurements, we assumed a linear variation of flux divergence from one stack to another. Because of safety considerations, the aircraft could fly no lower than about 70 m; however, we test the possibility of linear extrapolation of the measured fluxes to the surface (section 7b) with reasonable results.

The stacks were flown over the major divisions of the Gulf Stream (Fig. 1): the cold shelf water near the coast (Stack 1; E1), the western Gulf Stream front (Stack 2; E2), the Gulf Stream core (Stack 3; E3), and the eastern Gulf Stream front (Stack 4; E4) in order to investigate the changes between these major parts of the Gulf Stream.

b. Mission plan

In order to position the turbulent flux stacks the Electra flew about 100 m below cloud base at zero drift to the eastern edge of the Gulf Stream. Using maps of sea surface temperature (SST; obtained shortly before takeoff) that showed Gulf Stream mesoscale eddy structure, the stacks were positioned using onboard readout of a downward-looking infrared radiometer that measured SST. In addition to vertical soundings obtained on descent into the experimental area and on ascent out of the area, two other soundings from 70 m to above cloud top were made at E2 and E4. The stacks were flown after reaching the eastern Gulf Stream front

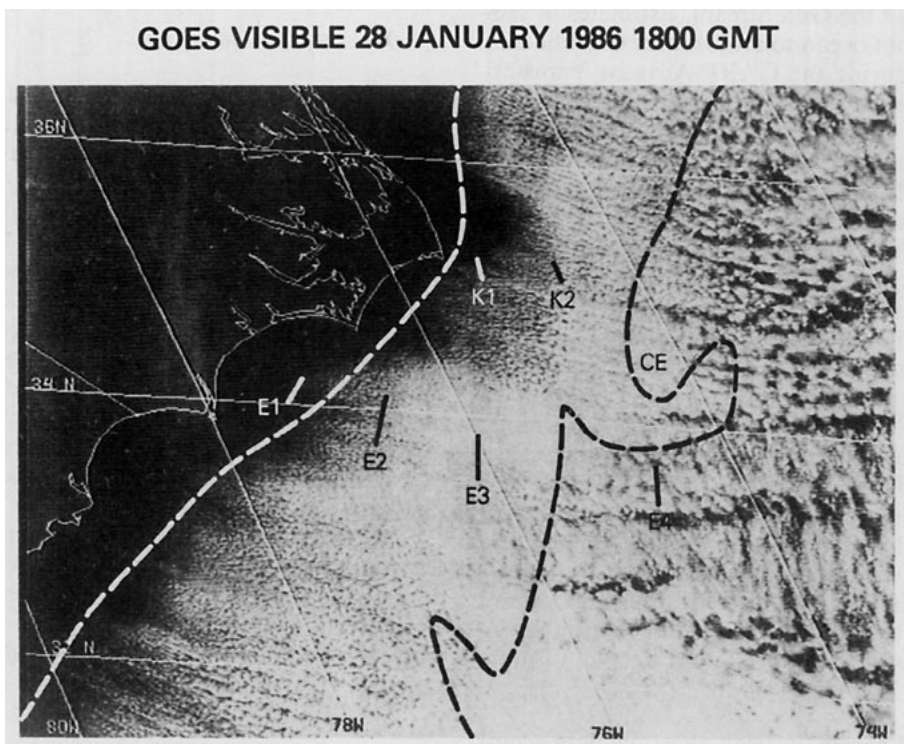

FIG. 1. Flight tracks of NCAR's Electra and King Air aircraft during the GALE cold air outbreak mission of 28 January 1986 superimposed on GOES visible imagery. Stacks of level legs were flown by the Electra at positions E1, E2, E3, and E4. The white dashed line demarcates the western Gulf Stream front and the dark dashed line the eastern Gulf Stream front. Figure courtesy of Dr. Shu-Hsien Chou, NASA Goddard Space Flight Center.

so that the sequence in time was E4, E3, E2, and E1. Stack E2 was near the RV *Cape Hatteras* which was steaming to a new station position at the time.

c. Data used in this study

The Electra aircraft data used include: once per second samples of wind vector, sea surface temperature, pressure, air temperature, absolute humidity, specific humidity, radar altitude, inertial navigation position, net infrared radiation (upwelling minus downwelling pyrgeometer values) and 20-per-second samples of horizontal and vertical wind components, air temperature, and absolute humidity. These data were supplemented by video camera imagery of the environment surrounding the aircraft (left, right, and forward) and notes taken by a dedicated group of student meteorological observers associated with the various universities participating in GALE.

The high-frequency samples of data gave excellent relative values but were not reliable as absolute values so the linear regression line, or trend obtained on a given level leg of a stack was removed so that

$$w = \bar{w} + w'$$

and

$$\Phi = \bar{\Phi} + \Phi' \qquad (2)$$

where the overbar indicates the linear trend for the level leg and the prime is a deviation from that trend line. Here w is the vertical velocity and Φ is a scalar quantity such as potential temperature (θ) or absolute humidity (ρ_v). These detrended values can be combined to form covariances, and covariances, one component of which is the vertical velocity, are used as estimates of vertical fluxes.

The fast response humidity measurement on the NCAR Electra is made using a Lyman-alpha hygrometer. The Research Aviation Facility of NCAR emphasizes the developmental nature of this instrument for which calibration has been difficult (Miller and Friesen 1985). Friehe et al. (1986) developed a scheme to calibrate the Lyman-alpha hygrometer using a slow response thermoelectric dewpoint measuring instrument with good absolute accuracy; a variation of this method (Grossman and Chou 1989) was used to produce fast response values of absolute humidity so that moisture flux could be estimated. However, even this reasonably straightforward method was limited by the meteorological conditions which accompany a cold air outbreak; namely, the air leaving the coast is very dry being equal to or even below 1 g m^{-3}. At these low values of absolute humidity, as pointed out in NCAR's data quality report[2] for this particular mission, the slow response dewpoint device begins to lose time-response and resolution. Our calibration efforts confirmed this, showing that the method would not work for stack E1. By E2 the air had moistened enough so that the thermoelectric device worked properly. However, as described in section, precipitation was encountered at stack E4 which probably compromised the flux measurements (and possibly some portions of the slower response temperature and humidity time series as well). Seeing little variation of Lyman-alpha calibration coefficient with height or between E2 and E3, we chose to average all values of the coefficients and use that average (the value 2.066 g m^{-3} volt^{-1}) to calibrate the Lyman-alpha data.

Since the Lyman-alpha hygrometer was calibrated with respect to absolute humidity, the vertical fluxes were also in terms of absolute humidity. These absolute humidity fluxes were adjusted for correlated temperature and humidity fluctuations according to the correction set out by Webb et al. [1980; see their Eq. (25)].

3. Synoptic overview and mission meteorological conditions

a. Synoptic overview

The following description has been abstracted in part from the excellent synoptic description given by Mercer and Krietzberg (1986) in the GALE Field Program Summary; another excellent summary concentrating on upper-air conditions is given by Uccellini et al. (1986).

During 27 January a complex arrangement of wind shift lines and pressure troughs were evident in the cold air behind a developing cyclone that was moving through North Carolina. Early on the 28th these mesoscale systems appeared to merge east–northeast of Cape Hatteras, a common place for the development of intense East Coast storms. This merger coincided with a period of offshore cyclogenesis with the storm moving rapidly to the northeast. Immediately after the cyclogenesis event, coincident with the aircraft mission, a very cold arctic air mass pushed into North Carolina and rapidly moved off shore and over the Gulf Stream. Temperatures at 500 mb were −40°C and as low as −27°C at 850 mb while surface air temperatures were below 0°C. The cold temperatures observed at 850 hPa fall well below the extreme cold air outbreak criterion of −15°C set by Konrad and Colucci (1989) in their study of extreme cold air outbreaks. The extensive surface network mounted for GALE showed that during the period of the aircraft mission offshore flow was relatively steady in the vicinity of the mission area but was changing with time to the north. Coastal and inland observations showed that the airmass was very dry (1 to 2 g m^{-3} absolute humidity).

[2] The NCAR aircraft data quality reports for GALE missions are available from the GALE Data Center, Dept. of Physics and Atmospheric Science, Drexel Univ., Philadelphia, PA 19104 or from NCAR/RAF, POB 3000, Boulder, CO 80307.

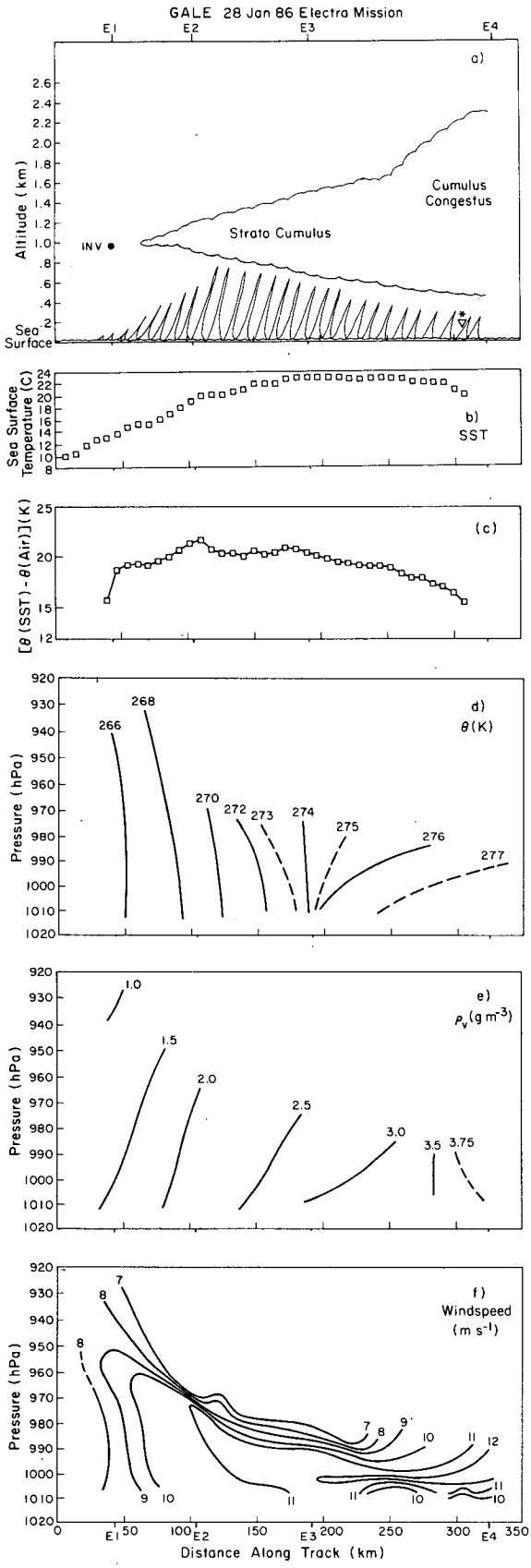

FIG. 2. Cross sections along aircraft track during GALE, NCAR Electra Mission, 28 January 1986. Flux stacks are marked as E1, E2, E3, and E4 corresponding to Fig. 1. (a) Schematic of cloud and steam plume conditions. Dot marks inversion level at E1. Lines showing cloud are from LCL computations (bottom) and NASA Electra lidar-NCAR Electra data (top). Shaded area shows uneven cloud bases; (b) sea surface temperature from infrared radiometer; (c) sea minus air potential temperature difference; (d) potential temperature corrected for diurnal variation; (e) absolute humidity; and (f) windspeed.

b. Mission meteorological conditions

GOES visual (Fig. 1) and infrared imagery (viz. Mercer and Krietzberg 1986) shows that most of eastern North Carolina was clear for the period of the mission. This clear zone extended off shore about 60 km. As the aircraft moved about 15 km off shore faint wisps of condensate (which we will call "steam") could be seen on the ocean surface, these wisps of steam became progressively more numerous and distinct as the NCAR Electra flew under a scattered stratocumulus deck which became broken and finally overcast about 120 km offshore (a schematic of cloud conditions encountered is shown in Fig. 2a). The beginning of the overcast nearly coincided with the western Gulf Stream front. As the aircraft proceeded to the eastern edge of the Gulf Stream mean cloud base (estimated as the lifting condensation level, LCL) lowered from about 930 m to about 460 m (Table 1). At the same time, our soundings and visual observations at stacks E2 and E4 as well as downward-looking lidar and visual observations from the NASA Electra aircraft (Palm et al. 1988; Melfi, personal communication 1986) indicated that cloud top was growing rapidly downstream and that cumulus congestus were present in the area around E4. On the eastern edge of the Gulf Stream (E4) snow showers were encountered.

The zone under the overcast area was full of steam. The steam spectacularly displayed convective motions within the subcloud layer with plumes of condensate often reaching from the sea surface into the cloud layer (Fig. 3); in addition numerous waterspouts were observed. It was often hard to distinguish between waterspouts and steam "plumes," which often burst from the white-capped ocean surface, and progressed so rapidly to cloud base that it appeared there was a direct connection between surface and cloud. Many of the steam plumes were rotating and therefore had the appearance of vortex tubes; however, there were plumes which did not appear to rotate. Sometimes the plumes were strongly sheared while at other times they were nearly vertical. As expected, the frequency of occurrence of steam plumes was tied to the sea surface temperature with the highest frequency of plumes over the area east of the western Gulf Stream front to the central part of the Gulf Stream where the sea–air potential temperature (θ) difference was 23 K (Fig. 2c). The plumes often occurred in "families" reminiscent of

TABLE 1. Sea surface temperature, sea–air potential temperature difference, Monin–Obhukov stability, and turbulence scaling parameters for NCAR Electra Stacks, 28 January 1986 (Time in decimal hours; L, w_*, u_*, θ_{v*}, ρ_{v*}, are from Chou and Zimmerman 1989).

Stack	Distance along track (km)	Elapsed time (hrs)	SST (C)	Sea–air diff (K)	LCL (m)	Z_i (m)	$-Z_i/L$	w_* (m s^{-1})	u_* (m s^{-1})	θ_* (K)	ρ_{v*} (g m^{-3})
E1	42.8	1.43	14.3	17.8	1500	960	8	1.81	0.66	0.094	0.072
E2	104.5	3.22	19.9	23.4	930	1200	5	2.25	1.07	0.129	0.111
E3	190.7	5.40	22.9	23.5	670	1500	8	2.56	0.95	0.120	0.116
E4	324.5	8.59	20.3	13.7	460	2300	33	2.61	0.61	0.092	0.084

Konrad's (1970) clear air radar observations of the convective boundary layer off of the East Coast; however, there were many "orphans" as well. Even with the elevated sea–air temperature differences, wind speeds were high enough (10 to 12 m s^{-1}) to be associated with roll vortices (Woodcock 1940; Grossman 1982; see also section 5). On some crosswind legs the airborne observers indicated that steam plumes occurred in fairly regularly spaced clumps, which may be associated with modulation by large-scale eddies (i.e. roll vortices); satellite imagery (Fig. 1) showed cloud streets occurring north and south of the Electra mission area.

4. Mean conditions

The mean meteorological conditions following the 1035L coastal air mass are shown as cross sections of cloud layer thickness (Fig. 2a), sea surface temperature (Fig. 2b), sea–air potential temperature difference (Fig. 2c), potential temperature (Fig. 2d), absolute humidity (Fig. 2e), and windspeed (Fig. 2f). Because land diurnal variability affected the temperature measured at each stack, we removed the diurnal variation from the measured potential temperatures that were used in the cross section as follows. We calculated the average diurnal variation at the coast using surface data from three automatic weather stations (NCAR's Portable Automated Mesonet; PAM) positioned along the coast near Wilmington and which bracketed the streamline flown by the Electra. This diurnal variation was the same as that measured by coastal zone buoys positioned near the mission flight track. The average potential temperature at the coast for the time of our budget analysis (1035L; see sections 6 and 7) was 265.5°C. The advection time was calculated along streamlines from the coast, and potential temperature was referenced to the mean time air left the coast (1035L) that was subsequently measured at stack S2 (1348L).

FIG. 3. Picture of subcloud layer from left window (looking north) of NCAR Electra near stack E3 during 28 January 1986 GALE cold air outbreak mission. Photo by Ms. Nancy Lang.

The potential temperature increased downstream by about 12°C with most of the increase (8°C) occurring before the Gulf Stream core area. When the stack values of θ were corrected for diurnal variation at the coast the resulting θ profiles had varying degrees of instability with height; E1 and E2 were nearly neutral but E3 and E4 became progressively more unstable (Table 2). Moisture content, shown as isopleths of absolute humidity, had an overall increase with fetch of almost 3 g m^{-3} with over 80 percent of the increase occurring before the Gulf Stream core. Moisture generally decreased with height before the core and was nearly constant with height to the east so virtual potential temperature had a vertical profile qualitatively similar to θ. Cloud base (and the lifting condensation level) decreased with fetch in this dry, cold, boundary layer, as the effect of moistening outweighed the warming of the subcloud layer. The sharpest horizontal gradient of sea–air temperature difference occurred from east of the western Gulf Stream front to the middle of the Gulf Stream. This is consistent with our observation that this was also the area where most of the heating and moistening of the airmass occurred. The maximum sea–air temperature difference (23 K) did not occur over the core of the Gulf Stream but rather to the west near the position of stack E2, which was near the western Gulf Stream front. The sea–air temperature difference slowly decreased to the east of the Gulf Stream core.

Windspeed increased by about 4 m s^{-1} from E1 to E4 with most of the increase occurring before the Gulf Stream core. A broad low-level wind maximum was identified centered about the *middle of the subcloud*

TABLE 2. Mean quantities for GALE 28 January 1986 cold air outbreak Electra Mission (Time in decimal hours; ? indicates data may be compromised by sensor wetting).

Stack	Leg average time (h)	Altitude (m)	Pressure (hPa)	Windspeed ($m\ s^{-1}$)	ρ_v ($g\ m^{-3}$)	q ($g\ kg^{-1}$)	Measured θ (K)	Diurnal temp correction (K)	Corrected θ_c (K)	Flux θ ($W\ m^{-2}$)	Flux ρ_v ($W\ m^{-2}$)	Net longwave radiation ($W\ m^{-2}$)
E1	15.28	458	961.0	9.6	1.279	1.014	268.38	−3.43	264.95	60	177	133
	15.13	292	981.4	8.4	1.317	1.022	268.24	−3.27	264.97	144	240	129
	14.96	144	999.8	8.3	1.364	1.062	268.08	−3.09	264.99	151	264	135
	14.82	68	1009.5	7.9	1.394	1.080	268.03	−2.95	265.08	230	337	134
Layer mean	**15.05**			**8.6**	**1.339**	**1.045**	**268.18**		**265.00**			
E2	14.07	404	967.8	11.4	1.973	1.569	268.37	−0.28	268.09	173	479	88
	13.87	202	993.0	9.9	2.000	1.570	268.18	−0.07	268.11	248	509	101
	13.70	132	1001.5	10.9	2.000	1.562	268.11	0.10	268.21	303	542	103
	13.55	69	1009.5	9.7	2.134	1.635	268.00	0.26	268.26	375	671	95
Layer mean	**13.80**			**10.5**	**2.027**	**1.584**	**268.17**		**268.17**			
E3	12.97	197	992.8	11.3	2.882	2.273	270.87	3.16	274.03	235	705	63
	12.83	136	1000.0	11.9	2.957	2.330	270.77	3.30	274.07	297	731	65
	12.68	78	1008.9	11.1	3.020	2.363	270.90	3.46	274.36	364	799	72
Layer mean	**12.83**			**11.4**	**2.953**	**2.322**	**270.85**		**274.15**			
E4	11.82	177	994.4	12.2	—	—	273.44?	2.86?	276.30?	172?	561.0?	48
	11.96	144	998.6	12.6	3.969?	3.123?	273.73?	2.82?	276.55?	222?	673.0?	55
	12.09	70	1007.0	10.1	4.05?	3.160?	273.89?	2.78?	276.67?	257?	498.0?	66
Layer mean	**11.96**			**11.6**	**4.001**	**3.142**	**273.69**		**276.51**			

layer; it appeared to extend into the cloud layer between E3 and E4, coincident with the onset of convective activity.

Previous observations over the ocean indicate that the low-level wind maxima are located near the inversion level. Kuettner (1959) points out that such low-level maxima are often observed (along with banded cloud structure) in cold air outbreaks over the Gulf Stream. Shepard and Omar (1952), Kuettner (1959), and Grossman and Friehe (1986) suggest that in some situations in the marine boundary layer a low-level wind maximum is the result of frictional retardation of the wind below the maximum and geostrophic shear, causing the decrease of wind above the maximum. Data from the Electra indicate the presence of a wind maximum near the inversion in addition to the one observed in the subcloud layer. This situation is clearly different than the one described by Kuettner (1959) and Grossman and Friehe (1986) so some other mechanism(s) must be sought for the explanation of the subcloud layer wind maximum.

Vertical profiles of wind direction within the subcloud layer show backing near the coast at E1 (Fig. 4) while at E2, E3, and E4 wind direction appeared to be constant with height. Kuettner (1959) points out that the nearly constant wind direction with height observed in cold air outbreaks may be the result of a balance between frictional veering of the wind and backing resulting from cold advection.

5. Turbulence conditions

Turbulence conditions for a less intense cold air outbreak during the Mesoscale Air Sea Exchange (MASEX) experiment have been reported by Chou et al. (1986), who compared their results to those from the even weaker cold air outbreaks observed during the AMTEX. Chou and Zimmerman (1989) describe the structure of the buoyancy flux measured by the Electra on this mission and find it in good agreement with observations made during AMTEX and the convective boundary layer over dry land, but different from a tradewind boundary layer. They point out that the main difference between the extreme cold air outbreak

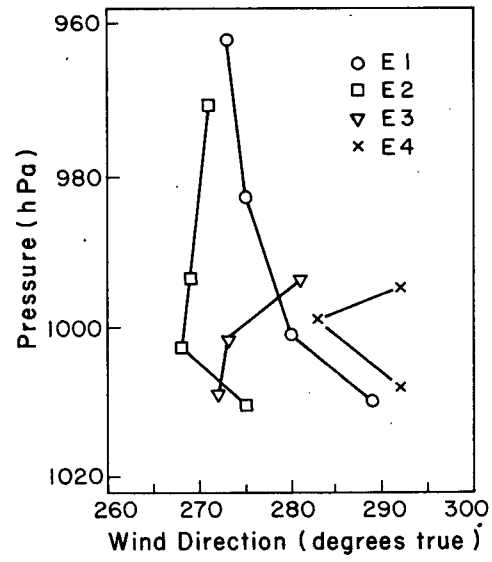

FIG. 4. Vertical profiles of mean wind direction. GALE, NCAR Electra Mission, 28 January 1986.

case and the tradewind case is that for the cold air outbreak the buoyancy is primarily the result of temperature differences owing to the large air–sea temperature difference, while in the trades the air–sea temperature difference is small and buoyancy is mainly due to water vapor anomalies.

Data relating to each stack such as average sea surface temperature, potential temperature difference between the sea and air, Monin–Obhukov stability, and various scaling parameters relating to turbulence are presented in Table 1. Values for stack means, standard deviations and fluxes of temperature and absolute humidity are presented in Tables 2 and 3 along with correlation coefficients for the temperature and moisture flux as well as the temperature–humidity covariance. Stack E4 was flown in convective snow showers subjecting the thermodynamic measurements to wetting, thus making them suspect. As a result, while mean values may be representative, variances and fluxes may be unrepresentative.

We adopt the convention of Chou and Zimmerman (1989) which places the (scaling) height of the mixed layer, Z_i, at the top of the cloud layer. This differs from shallow, cumulus topped boundary layer scaling over land and ocean, where Z_i is typically the top of the subcloud layer. In this extreme cold air outbreak case the depth of the subcloud layer is shrinking with fetch, indicative of heating not compensating for moistening of the subcloud-layer air; this occurred while the top of the stratocumulus overcast is increasing with fetch, typical of a boundary layer being warmed and moistened from below. No distinct potential temperature transition layer (often seen in shallow, cloudy marine boundary layers) between the subcloud and cloud layer was seen which may be indicative of strong coupling between the cloud and subcloud layers. A strong inversion capped the top of the cloud layer. Thus this boundary layer falls into the category of boundary layers that include the cloud layer as suggested for convective cloud clusters by Zipser and LeMone (1980).

Estimates of stability centered on the virtual potential temperature gradient and the ratio of the boundary layer depth, Z_i, to the Monin–Obhukov length

$$L = u_*^3 \theta_v / gk\theta_{v*} \qquad (3)$$

where u_* is the friction velocity ($\sqrt{\overline{u'w'}}$), g is the gravitational acceleration, k is the von Karman constant, θ_v is the virtual potential temperature, and θ_{v*} is the surface-layer scaling parameter for virtual potential temperature. Since θ_{v*} was negative for all stacks, the stability parameter, Z_i/L (Table 1), indicated unstable conditions. According to LeMone (1973) and Grossman (1982), Z_i/L estimates made at stacks E1, E2, and E3 were in a range of values associated with roll vortices which were probably modulating the convective cell distribution; while at stack E4 the value of Z_i/L was associated with a random spatial distribution of convection. The virtual potential temperature gradient showed that the subcloud layer was slightly unstable for E1 and E2, and became progressively more unstable for E3 and E4; this is qualitatively similar to observations in cold air outbreaks from the coast of China (Riehl 1979).

a. Standard deviation profiles

Alongwind windspeed fluctuations (σ_u; Fig. 5a) increased with fetch reaching a maximum of almost 2 m s^{-1} at E3 over the Gulf Stream core with no consistent variation with height. Cross-stream windspeed standard deviations (σ_v; Fig. 5b) also increased with fetch and generally decreased with height.

Further supporting the idea of a closely coupled cloud and subcloud layer (where Z_i is the top of the cloud layer) is the vertical profile of vertical velocity (Fig. 6a) that shows a maximum at about $0.3Z_i$ at E1 and E2, comparable to other studies of the convective boundary layer (Lenschow et al. 1980). At E3 and E4

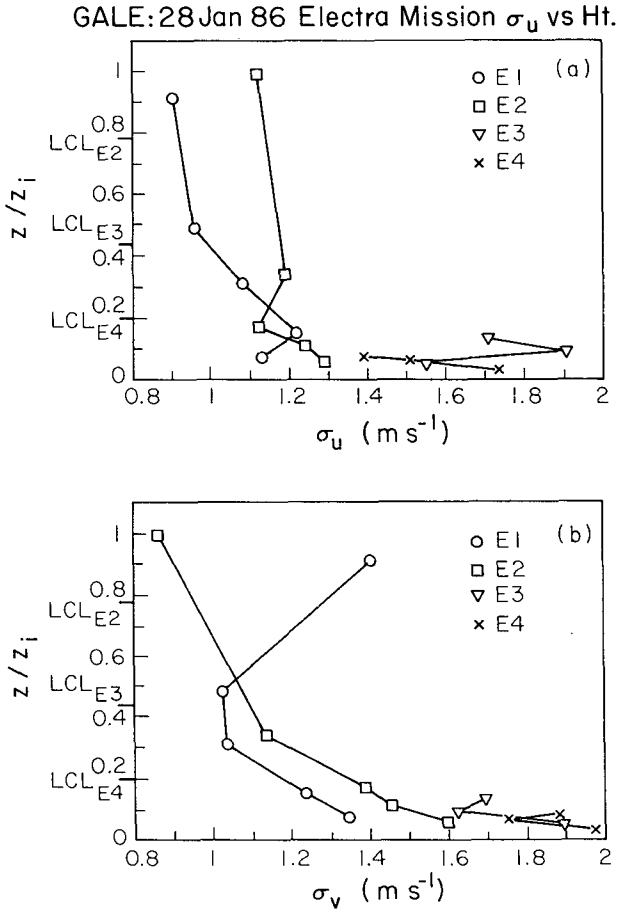

FIG. 5. Vertical profiles of the standard deviation of detrended (a) alongstream wind (u) departures from leg average; (b) cross stream wind (v) departures from leg average. GALE, NCAR Electra Mission, 28 January 1986.

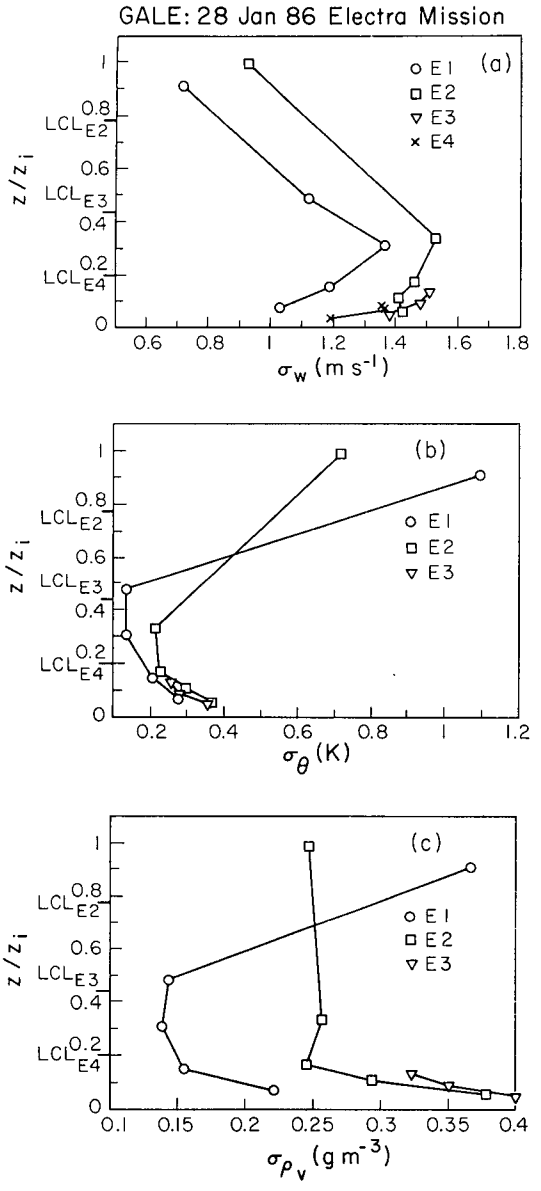

FIG. 6. Vertical profiles of the standard deviation of detrended (a) vertical velocity (w); (b) potential temperature (θ) departure from leg average; (c) absolute humidity (ρ_v) departure from leg average. GALE, NCAR Electra Mission, 28 January 1986.

no subcloud layer maxima were observed though fluctuations increased with height to cloud base ($0.1z/Z_i$). Values were quite high (between 1 and 1.5 m s^{-1}) and increased with fetch to E3. Potential temperature and moisture fluctuations (Figs. 6b, c) decrease with height with the decrease behaving like other convective boundary layers (Chou and Zimmerman 1989). The increase in θ fluctuations around Z_i is consistent with entrainment processes bringing potentially warmer and drier air into the subcloud layer. The intensity of the θ fluctuations increased slightly with fetch, in contrast with humidity fluctuations which increased quite a bit more (almost 100 for moisture compared to 50 for θ between E1 and E3).

b. *Flux profiles*

The flux profiles of sensible and latent heat (Fig. 7) are an important input to the budget analyses that follow (sections 6 and 7). The observed decrease of fluxes with height during cold air outbreaks was first noted by Bunker (1960). While Chou and Zimmerman (1989) indicated that a composite of virtual potential temperature fluxes from both the Electra and King Air missions show the average flux near Z_i to be about -0.24 of the average surface flux; there was quite a bit of scatter in the data near Z_i. We normalized the sensible and latent heat fluxes for each stack with a "surface" flux value obtained from linear regression and performed a linear regression against z/Z_i on the composite of all stacks. The extrapolated "surface" flux differed from the flux measured at 70 m by only a few percent. From the regression of the normalized fluxes we found that the inversion height flux was -0.18 ± 0.14 and -0.06 ± 0.06 of the extrapolated surface fluxes for sensible heat and latent heat, respectively. Correlation coefficients for the regressions were high: 0.91 for sensible heat and 0.98 for latent heat. For the flux of virtual potential temperature the inversion flux

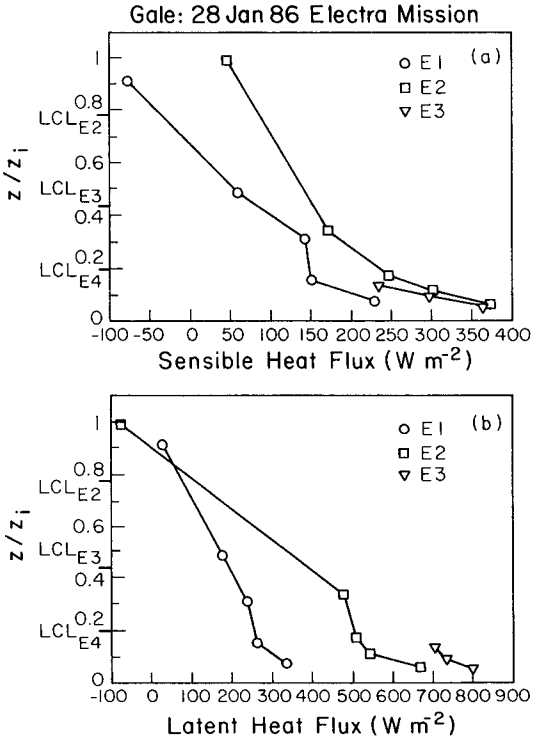

FIG. 7. Vertical profiles of sensible and latent heat flux for GALE, NCAR Electra mission, 28 January 1986.

was -0.17 ± 0.13 of the "surface" flux; the regression had a correlation coefficient of 0.92.

The total (sensible plus latent heat) low-level (70 m) heat flux nearly doubled from 567 W m^{-2} at E1 to about 1100 W m^{-2} at E2 and E3. These values are comparable to a regional average of 720 W m^{-2} estimated from a budget evaluation, using aerological data over the Kuroshio region, by Ninomiya and Akiyama (1976). The fluxes at E2 and E3 are among the highest ever observed in the marine boundary layer (Chou et al. 1986; Lenschow et al. 1980; Grossman 1982; Augstein 1979; Bane and Osgood 1989). Further estimates of surface fluxes from these low-level measurements are covered in sections 7b, c.

The heat flux decreased with height (flux convergence which would tend to warm the subcloud layer) and at E1 the flux convergence was slightly greater than that measured in AMTEX and MASEX; however, at E2 and E3 it was greater than twice those previous measurements. The latent heat flux convergence was comparable to the sensible heat flux convergence at stack E1 (Table 4a). At stacks E2 and E3 the latent heat flux convergence was about 80 of the sensible heat flux convergence. Both sensible and latent heat flux convergence increased from E1 to E3. The scanty data we have at E4 suggested that both sensible and latent heat flux convergence decreased after E3.

Finally, we note that for E1, E2, and E3 the flux profiles appear to be consistently nonlinear with height. If there were no counteracting vertical variation of sinks of sensible heat and moisture, then this would suggest that sensible heat and moisture were being accumulated at a faster rate near the 70 m level than near cloud base; this would tend to destabilize the layer. However, because of the uncertainty in the flux measurements, especially near cloud base, we have assumed a linear decrease of fluxes over the layer thickness for estimates of the flux divergence term in the budget estimates (section 6).

c. *Correlation coefficients (Table 3)*

When applied to flux covariances the correlation coefficient can be viewed as flux transport efficiency since it is the ratio of actual flux to potential flux. The lowest level correlation coefficients for temperature and humidity flux are among the highest ever observed. Low-level values at E2 and E3 are slightly less than those at E1. Following Grossman (1984), these high correlations suggest that there was very little mixing between upward and downward moving convective cells in the lowest layers (see also Chou and Zimmerman 1989). At E1, E2, and E3 the correlation coefficient for sensible heat flux decreased with height while a similar decrease for latent heat correlation coefficient was only noticed at E1 (where there were few steam plumes). At E2 and E3, which had many steam plumes, the latent heat-flux correlation coefficient was nearly constant with height. This suggests that there was progressively more mixing with increasing height for potential temperature than for absolute humidity. In a moist boundary layer dominated by convective processes very high positive correlation between temperature and humidity is expected at the very lowest levels with a decrease to very high negative correlation near the inversion; this was observed.

6. Subcloud layer streamline budgets of sensible and latent heat

The mission was designed to evaluate the streamline budgets for heat and moisture in the subcloud layer. Two Lagrangian (e.g., moving with the mean flow) methods of evaluation will be presented. The first, discussed in this section, looks at the layer-averaged sensible and latent heat budgets separately. The second method, covered in section 7, combines those budgets in graphical form in $\theta - q$ space with the sensible and latent heat budgets as components of a vector repre-

TABLE 3. Turbulence quantities for GALE 28 January 1986 cold air outbreak Electra Mission (? indicates data may be compromised by sensor wetting).

Stack	Altitude (m)	z/Z_i	σ_u (m s^{-1})	σ_v (m s^{-1})	σ_w (m s^{-1})	σ_θ (K)	σ_{ρ_v} (g m^{-3})	$r_{w\theta}$	$r_{w\rho_v}$	$r_{\theta\rho_v}$
E1	458	0.48	0.96	1.03	1.12	0.14	0.143	0.37	0.46	0.39
	292	0.31	1.08	1.04	1.37	0.14	0.138	0.58	0.55	0.72
	144	0.15	1.22	1.24	1.19	0.21	0.154	0.46	0.59	0.67
	68	0.07	1.13	1.35	1.03	0.28	0.221	0.60	0.67	0.92
E2	404	0.34	1.19	1.14	1.53	0.22	0.257	0.40	0.53	0.39
	202	0.17	1.12	1.39	1.46	0.23	0.245	0.57	0.58	0.74
	132	0.11	1.24	1.46	1.41	0.30	0.293	0.55	0.53	0.83
	69	0.06	1.29	1.60	1.42	0.37	0.378	0.55	0.51	0.87
E3	197	0.13	1.71	1.70	1.51	0.26	0.323	0.46	0.60	0.56
	136	0.09	1.91	1.63	1.48	0.28	0.351	0.55	0.56	0.62
	78	0.05	1.55	1.90	1.38	0.36	0.402	0.57	0.60	0.74
E4	177	0.08	1.39	1.89	1.36	0.66?	0.335?	0.15?	0.52?	0.33?
	144	0.06	1.51	1.76	1.37	0.35?	0.491?	0.36?	0.41?	0.17?
	70	0.03	1.74	1.98	1.19	0.42?	0.437?	0.40?	0.39?	0.28?

sentation. The two methods are complementary in that they give unique looks at the air–sea interaction associated with an extreme cold air outbreak, highlighting its different aspects.

As stated before, the budgets were referenced to a particular time (see section 4) in order to remove the influence of diurnal variability at the coast, thus isolating the role of air–sea interaction. This diurnal correction involves two key assumptions: 1) the diurnal variation of temperature measured at the coastal PAM surface stations is representative of the subcloud layer; 2) the diurnal variation in absolute humidity and windspeed was negligible. We also assumed that all variables had a linear variation between stacks, and with height. Lagrangian advection times were estimated by dividing the distance between stacks by the mean windspeed over that interval.

As mentioned before, stack E4's flux data was questionable, so the segment E3–E4 was not included in the budget evaluation discussed in this section and section 7a. The turbulent flux divergence terms were found by averaging the flux difference between the lowest and highest flight level at each stack, divided by the average altitude separation. The radiative flux divergence term was determined by a linear regression of net longwave radiation measurements from upward- and downward-looking pyrgeometers. The budget results are presented in Table 4 in three ways: in Table 4a results are shown in units of W m^{-3} and as a percent of the Lagrangian time change between stacks; in Table 4b results are shown as a flux difference (in W m^{-2}) over the stack-pair, average layer thickness; that difference is also shown as a percentage of the stack-pair average low-level flux measured by the aircraft.

One of the main goals of this research was to estimate the relative importance of the components of the sensible and latent heat budgets. The results of the sensible and latent heat budgets between stacks E1–E2 and E2–E3 are presented in Table 4. From Table 4 we see that for the sensible heat budget, turbulent flux convergence is a major term accounting for from 74 to 80 percent of the Lagrangian temperature change while radiative flux convergence was small but significant (approx. 3 to 5 percent); a net warming source was evaluated as a residual that slightly increased from 17 percent between E1–E2 to 21 percent between E2–E3. This residual warming may be due to net condensation in the layer which is consistent with steam observed rising from the ocean surface into cloud base (Fig. 3).

For the latent heat budget the turbulent flux convergence greatly exceeded the Lagrangian moisture change, leaving a substantial net drying as a residual. This residual was 82 percent of the Lagrangian moisture change between E1–E2, and 111 percent of the moisture change between E2–E3. A residual drying could also be due to condensation. The spatial trend, more drying in E2–E3, is consistent with the presence of more steam plumes in that region compared to E1–E2, which

TABLE 4a. Inputs to sensible and latent heat budget analysis NCAR Electra GALE Mission, 28 January 1986.

Stack pair	δt	Scaling speed	$\delta\rho_v$	$\delta\theta$	$\delta\theta/\delta t$	$\overline{\partial w'\theta'}/\partial z$	∂ net rad/∂z	Sensible heat residual	$\delta\rho_v$	$\partial\rho_v/\delta t$	$\overline{\partial w'\rho_v}/\partial z$	Latent heat residual
	(s)	(m s^{-1})	(g kg^{-1})	(K)	(W m^{-3})	(W m^{-3})	(W m^{-3})	(W m^{-3})	(g m^{-3})	(W m^{-3})	(W m^{-3})	(W m^{-3})
E1–E2	6481	.146	.540	3.17	.642	−.513	−.019	.110	.688	.267	0.486	−.219
% of	$\delta/\delta t$					80.0	3.0	17.0			−181.8	−81.8
E2–E3	7847	.102	.738	5.99	.991	−.729	−.052	.209	.937	.295	−.630	−.335
% of	$\delta/\delta t$					73.6	5.4	21.0			−211.0	−111.0
E3–E4	11 412	.050	.813	2.48	—	—	—	—	—	—	—	—

TABLE 4b. Sensible and latent heat budget components expressed as flux difference (W m^{-2}) over average layer depth (see text).

Stack pair	Δz (m)	$\delta\theta/\delta t$	$\partial\overline{w'\theta'}/\partial z$	∂ net rad/ ∂z	Sensible heat residual	$\partial\rho_v/\delta t$	$\partial\overline{w'\rho_v'}/\partial z$	Latent heat residual
E1–E2	363	233	−186	−7	40	97	−176	−79
% of average low level flux (sens heat = 302.5 W m^{-2}; latent heat = 304.8 W m^{-2})		76.9	−61.5	−2.3	13	19.2	−34.9	−16
E2–E3	227	225	−166	−12	47	68	−143	−75
% of average low level flux (sens heat = 369.5 W m^{-2}; latent heat = 735.0 W m^{-2})		60.9	−44.8	−3.3	13	−9.2	−19.5	−10

had a lower sea–air temperature difference compared to E2–E3 (Fig. 2c).

From the data in Table 4 the residuals of the sensible and latent heat budgets can be compared. Ideally they should have the same value since the two budgets are coupled through the source-sink terms; this was not the case for this analysis. For E1–E2 the sensible heat residual warming was only 50% of the residual drying while for E2–E3 warming was 62% of drying. This discrepancy is discussed further in section 7.

Our results suggest that net condensation occurred within the budget layer presumably as part of the formation and vertical advection of the steam plumes out of the layer. This net warming and drying suggests that evaporation of the subcloud layer condensate was limited during the period of observation. A possible constraint on evaporation could be the high (70–80 percent) relative humidities observed. Scanty aircraft data indicate that relative humidity apparently had a diurnal variation; it decreased as relatively warmer air was advected over the ocean from the coastal land area as the day progressed, since daytime heating would warm the air without substantially increasing its moisture content (in fact entrainment processes may decrease the moisture content of the boundary layer air over land). On the other hand, further cold advection from the continental interior or advection of the air over land cooled by nighttime radiation processes, should tend to increase relative humidity in the marine subcloud layer. Thus condensation heating may have a diurnal variation that our analysis could not have observed.

7. Graphical representation of subcloud layer budgets

Tables 2 and 4a show the stack-averaged specific humidity; q, potential temperature; θ, the diurnal correction referenced to stack 2; the corrected stack θ_c; the Lagrangian change $\delta\theta$; δq between stacks and an estimate of the Lagrangian advection time (δt) between stacks. This together with the flux data and boundary layer depths formed the input to the budget computations, as discussed above.

a. Stack-pair budgets

Following Betts (1984), Betts and Simpson (1987) and Boers and Betts (1988), we represent the thermodynamic budgets on a conserved parameter diagram. We shall use a (θ, q) diagram, so that the θ axis represents the sensible heat budget and q axis represents the latent heat budget. Figure 8 shows 2 stack-pair budgets: from E1 to E2 and from E2 to E3. As pointed out in section 6, these stack-pair budgets are mean budgets between the lowest (approx. 70 m) and highest (near cloud base) aircraft levels. For each pair of stacks, the budget equation (4) is first expressed in finite difference form as

$$\delta\phi = (\delta t/\delta z)(F_a - F_d) + (Q + S)\delta t \qquad (4)$$

where $\delta\phi$ is the Lagrangian change from one stack to the next ($\delta\theta$ and δq in Table 4a); F_a and F_d are fluxes at 2 levels δz apart, and δt is the advection time between the 2 stacks; $F_a - F_d$ represent the flux convergence term; Q is the radiative source term, and S is any other unresolved source such as condensation or evaporation within the layer. Except for the Lagrangian change term, the other terms in the equation were evaluated by using average values for the stack-pair (see section 6); consequently, the residuals also refer to a stack-pair average.

The points labeled 1, 2, and 3 in Fig. 8 represent the stack-pair mean (q, θ_c) values at stacks 1 to 3 (from

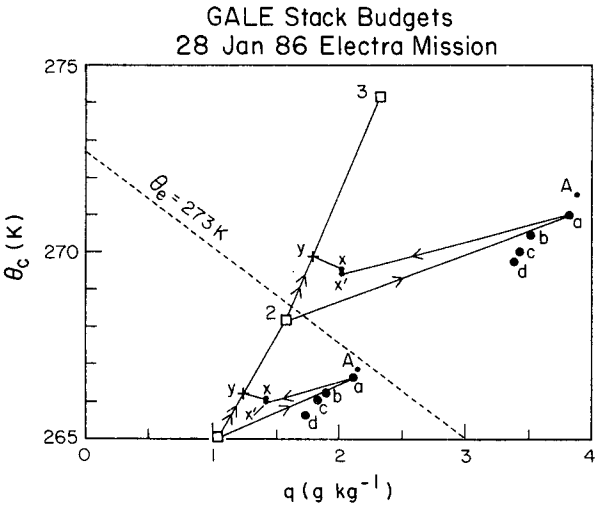

FIG. 8. Graphical representation of potential temperature and specific humidity budgets using aircraft stack data.

Table 2) and θ_c is the potential temperature corrected for the diurnal variation at the coast. The vector difference between these points is the Lagrangian change of θ_c and q of the layer as it crosses the Gulf Stream.

We then multiply (4) by $(\delta z/Z_B)$, where Z_B is our estimate of the average depth of the subcloud layer for each stack pair (we used the observed LCL in Table 1 for Z_B), to give

$$(\delta z/Z_B)\delta\phi_{12} = (\delta t/Z_B)(F_a - F_d) + (Q + S)(\delta z/Z_B)\delta t. \quad (5)$$

Figure 8 represents (5) as vector diagrams for the budget for each stack pair. Consider the Lagrangian change from E1 to E2 to which the subscripts for ϕ in (5) refer. The vector $1Y$ is the left-hand side of (5): the advective change between E1 and E2 scaled by the ratio of the budget layer thickness to the subcloud layer depth. The four vectors ($1a$, $1b$, $1c$, and $1d$) represent averaged aircraft fluxes corresponding to four levels in the subcloud layer (with mean heights of 69, 138, 247, 431 m). These are plotted as vector differences from 1 by multiplying the fluxes by the inverse of the scaling speed (Betts 1984; values in Table 4a), $\delta t/Z_B$. For E1, which had no cloud, the boundary layer (BL) depth Z_i was used for Z_B. We decided to use Z_B, not Z_i, for scaling on Figs. 8 and 9, because we have insufficient data to extrapolate the budgets above cloud-base. The points A are fluxes extrapolated to the surface and are discussed in section 7b to follow.

The vector $1X$, which represents the sum of the two RHS terms of (5), can be split graphically into the separate components by

$$1X = 1a + aX' + X'X \equiv 1a - 1d + X'X = (\delta t/Z_B)(F_a - F_d) + Q\delta t(\delta z/Z_B) \quad (6)$$

which represents the flux *difference* ($1a$ minus $1d$; the vector $X'A$ is the same as $1d$) across the stack plus the radiative term, which in this case is a small warming term, plotted as $X'X$ at constant q.

The residual vector XY represents errors in the data, or any unresolved source S [the last term in (5)]. For the stack pair E1–E2, the θ and q components of vector XY correspond to 13 and 16 percent of F_a (Table 4b), the average low-level aircraft fluxes of potential temperature and specific humidity, respectively. As noted in section 6, the residual XY vector represents a drying and a warming. The budget for the stack pair E2–E3 starts at point 2 on Fig. 8. The vector $2X$ is the flux difference plus radiative warming. The residual XY represents a warming that is about 12 percent of the average low-level potential temperature flux between stack pair E2–E3 and a drying that is 10 percent of the corresponding q flux.

We conclude that the residuals for both stacks represent unmeasured *drying and warming* as discussed in section 6. This suggests net condensation in the subcloud layer. Steam was observed rising off the surface. Unresolved condensation would appear in Fig. 8 as a vector *parallel* to a θ_e isopleth (θ_e = 273 K is shown for reference). The two stack-pair residuals, XY, have similar slopes less than that of the θ_e isopleth. This indicates that the moisture budget residual, in this case representing a drying of the layer, is greater than the potential temperature residual, which represents a warming. We see in Table 4b that for each stack pair the unresolved drying is almost twice the unresolved warming. We cannot account for this discrepancy between the residuals; however, considering the magnitude of the diurnal correction and the possible errors in the flux measurements, it seems likely that the residuals represent condensation in the subcloud layer which is then advected upward out of the stack volume and into the cloud layer (see Fig. 3). This is a significant contribution to the subcloud layer budget: it represents a heat source and a vapor sink corresponding (in energy units) to a liquid water flux difference across the stack thickness of approximately 60 W m^{-2}.

b. *Extrapolation to the surface*

The vectors $1a$, and $2a$ in Fig. 8 represent the low-level heat and moisture fluxes; they were measured 70 m above the surface and were associated with a sea–air temperature difference of order 20 K, steam coming off the surface, and some breaking waves. It seems appropriate to ask whether, under these conditions, surface fluxes can be estimated and whether they are consistent with results from simple bulk aerodynamic formulae. Figure 9 shows the same flux vectors $1a$, $2a$, and also our best estimate for the average low-level fluxes for stack pair E3–E4. For the moisture flux at

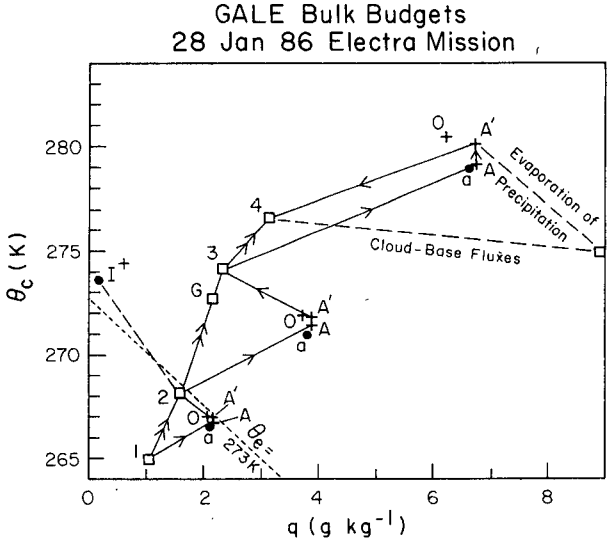

FIG. 9. Flux extrapolation to the surface and graphical representation of potential temperature and specific humidity budgets for entire subcloud layer.

E4 we used the average for the three legs since the flux measurements may have been compromised by precipitation wetting the sensors (Table 2). In Fig. 9 the vectors $1A$, $2A$, and $3A$ (indicated by solid lines) represent the aircraft fluxes extrapolated to the surface as follows (the point O is discussed in section 7c and A' in section 7d).

We express the budget between the surface and the lowest flight levels (a layer of stack-pair mean thickness, δz_{0a}) as

$$\delta z_{0a}(\delta\phi/\delta t) = (F_0 - F_a) + (Q_{0a} + S_{0a})\delta z_{0a}. \quad (7)$$

We shall *assume* that the radiative heating Q and the Lagrangian change, $\delta\phi$, for this layer close to the surface are the same as for the layer between 70 m and near cloud base and again scaled by $\delta t/Z_B$, so that the surface flux is given by:

$$(\delta t/Z_B)F_0 = (\delta t/Z_B)F_a + (\delta z_{0a}/Z_B)\delta\phi - (Q_{0a} + S_{0a})(\delta z_{0a}/Z_B)\delta t. \quad (8)$$

If we neglect S_{0a}, we obtain the extrapolated fluxes, marked A in Fig. 9, which are represented by the vectors $1A$, $2A$, and $3A$. Given the extreme meteorological conditions, our assumptions are questionable. This 70 m layer between the aircraft and the surface contains the very strong superadiabatic layer, where the radiative heating may be large; there may also be evaporation of spray into the dry air (see section 7c below).

c. *Bulk aerodynamic fluxes*

We also estimated the surface sensible and latent heat fluxes by the bulk aerodynamic method. Using the computation of the surface sensible heat flux as an example, for each stack pair we averaged the product of the measured mean low-level (approx. 70 m) windspeed, V_a, and the difference in θ between the surface (θ_s) and the low-level (θ_a) at each stack, and then multiplied that product by the bulk transfer coefficient, C_θ, for sensible heat. The same procedure was used for the latent heat flux, only using q instead of θ and the bulk transfer coefficient for latent heat (water vapor):

$$F_{0\theta} = C_\theta V_a(\theta_s - \theta_a) \quad (9a)$$

$$F_{0q} = C_q V_a(q_s - q_a). \quad (9b)$$

The points marked O represent the bulk aerodynamic fluxes at the ocean surface for $C_\theta = C_q = C$ with the values of C given in Table 5. Changing C alters the length of the flux vectors 1O, 2O, 3O but not their direction; so that agreement between the measured fluxes at the lowest flight level or the extrapolated fluxes (A) and the bulk aerodynamic formula (with equal transfer coefficients for sensible and latent heat fluxes) is not possible. This small anticlockwise rotation of the surface flux vectors (vectors 1O, 2O, and 3O were estimated from the bulk aerodynamic method) from the extrapolation of the aircraft measured fluxes (vectors $1A$, $2A$, $3A$) is the same for all stacks, and there are (at least) three possible explanations.

The first is that the transfer coefficient for moisture is greater than that for sensible heat. We computed transfer coefficients C_θ for sensible heat and C_q for moisture for each of the stack pairs which would match the aircraft fluxes extrapolated to the surface (Table 5). The mean value of C_q is 1.56 ± 0.05 and $C_\theta = 1.24 \pm 0.15$. There is a possibility that the radiative warming near the surface is large, much larger than measured between the aircraft stacks ($\approx 5 \times 10^{-5}$ K s^{-1}), and this has an impact on the θ profile in the superadiabatic layer, and hence on the transfer coefficients. Calculations with a simple radiative model suggest a large infrared heating rate in this layer, but the horizontally homogeneous clear sky models cannot be considered accurate for this surface layer that is partly filled with steam.

The second is that with the wind speeds ≥ 10 m s^{-1} there is some evaporation of spray from breaking waves into the dry air above. This takes latent heat from the air not the ocean when the spray evaporates: a process which conserves θ_e approximately, while increasing the atmospheric latent heat flux, and simultaneously reducing the sensible heat flux at some level where all of the spray evaporates (perhaps 20 m above the ocean). Although the windspeed at E1 is marginal for spray production (Fairall et al. 1989), there is a downstream increase in windspeed, and whitecaps were observed. In addition, the large sea–air temperature difference and energetic convection may facilitate the lifting and evaporation of any spray that forms beneath updrafts. So we made the *assumption* that the source S_{0a} in (8) was a spray-evaporation source term; and that this accounted for the difference between the extrapolated

TABLE 5. Drag coefficients and spray evaporation flux.

	C_θ $\times 10^{-3}$	C_q $\times 10^{-3}$	C $\times 10^{-3}$	Flux spray (W m^{-2})	Latent heat (W m^{-2})	Flux ratio (%)
E1–E2	1.35	1.59	1.48	35	522	6.7
E2–E3	1.32	1.59	1.48	52	757	6.8
E3–E4	1.06	1.51	1.33	83	705	11.4
Mean	**1.24**	**1.56**	**1.43**	—	—	**8.4**
Sigma	0.16	0.05	0.09	57	661	6

aircraft fluxes and the bulk aerodynamic estimates. If we set

$$S_{0a}\delta z_{0a} = F_0 - F_A \qquad (10)$$

where F_0–F_A is a vector at constant θ_e, then we can find O on Fig. 9 by adjusting the transfer coefficient C until we find a point O with the same θ_e as the corresponding A. This gives the values of C for each stack pair and the corresponding spray evaporation flux given in Table 5. The estimated evaporation of spray increases from the first to the last stack pair and corresponds to a liquid water flux that ranges (in energy units) from 35 to 80 W m^{-2} or 7 to 11 percent of the latent heat flux extrapolated to the surface (F_a). This mean bulk transfer coefficient of $1.43 \pm 0.09 \times 10^{-3}$ fits other observations over the ocean (Greenaert et al. 1986; Sheppard et al. 1972; Dunckel et al. 1974). If this estimate is correct, then the evaporation of spray dominates over the steam condensation close to the surface and is a significant component of the surface fluxes. The third possibility is that the aircraft moisture flux measurements are in error and are too large.

In summary we interpret Fig. 9 as follows. The points O represent the surface sensible and latent heat fluxes given by the bulk aerodynamic formula with the coefficients C in Table 5. There is also a flux of spray, which evaporates in the air and dominates over the near surface steam condensation giving a resultant flux vector A, that represents near surface conditions. The point labeled "a" represents the stack-pair average of fluxes measured from the aircraft during the low-level (70 m) legs. The flux difference between A and a is just sufficient to balance the Lagrangian change for this shallow layer and the radiative warming extrapolated from the aircraft measurements.

We have used a different scaling speed ($Z_B/\delta t$) (see Table 4a) for the budgets between each pair of aircraft stacks. This ties the budgets to the actual vector change 12, 23 and 34 between the stacks, as plotted on the figures. This is only a *convention* (we could have scaled the vectors 12 etc as well). One consequence of this choice-of-scaling factor is that the plotted surface flux vectors (1A etc.) increase in length as the corresponding scaling speeds decrease while the estimated surface fluxes increase from E1 to E3 and then decrease to E4.

d. Subcloud layer budget

The budgets for the layer corresponding to the aircraft measurements were presented in sections 6 and 7a. Figure 9 shows the budget for the entire subcloud layer. Since we only have adequate data for the horizontal legs in the subcloud layer, we must assume that the advective changes 12, 23, and 34, determined by the stack layer averages, are representative of the change for deeper layers. We have already made this assumption in section 7c when extrapolating the stack layer $\delta\phi/\delta t$ into the superadiabatic surface layer. We now extrapolate $\delta\phi/\delta t$ upward to cloud-base. We feel this is reasonable because the subcloud layer is internally coupled by strong vertical mixing, since the observed vertical thermodynamic gradients are small (see introduction to section 5).

In Fig. 9, the subcloud layer budgets are represented by the three quadrilaterals, 1AA'2, 2AA'3 and 3AA'4, marked with solid lines. The scaled budget equation is

$$\delta\phi = \delta t/Z_B(F_A - F_B) + (Q + S)\delta t$$

$$= (\delta t/Z_B)F_A + Q\delta t + (S\delta t - F_B(\delta t/Z_B)). \qquad (11)$$

For the stack pair E1–E2 the LHS of (11) is the vector 12; 1A is the first RHS term (the near surface flux); AA' is the second RHS term (the small radiative warming of the subcloud layer which increases θ with no change in q); and the vector A'2 is the sum of the cloud-base flux, F_B, and any unresolved source term in the subcloud layer (excluding the evaporation of surface spray, which is included in F_A). Between E1 and E2 the cloud layer forms, but it is still thin at E2 and not precipitating, so that there is probably no contribution from evaporation of precipitation falling into the subcloud layer. There may be condensation in the convective cells rising off the surface which is carried up to cloud base. The other major term in the vector A'2 is the unknown flux at the stack-pair average cloud-base (we used inversion height at E1 in lieu of cloud-base). A'2 is a vector almost parallel to the θ_e isopleths (θ_e = 273 K is shown for reference) representing a substantial flux of sensible heat (warming) and moisture (drying), but almost no θ_e flux. The air above the BL for E2 had thermodynamic properties indicated by point I^+. The vector A'2 is almost parallel to 2I^+; so it is roughly consistent with entrainment of air with properties I^+.

The subcloud budget between E2 and E3 is qualitatively similar to the first. The BL is still not precipitating, and the vector A'3 represents a warming and drying of the subcloud layer: it is not quite parallel to a θ_e isopleth (the drying exceeds the corresponding warming as noted before). There are again two possible contributions, which we cannot separate: a heat and vapor flux associated with a slightly unstable θ_e structure through cloud-base, and a source term associated with net condensation in the subcloud layer, advected across cloud-base in convective cells (Fig. 3). The budgets between E1–E2 and E2–E3 are quite similar to each other and to the stack-pair budgets in Fig. 8. Assuming that the stack-pair budget residuals represent condensation, then extrapolating them through the whole subcloud layer depth (by multiplying by Z_B/δ_z), we can estimate that between 50 and 60% of the vectors A'2 and A'3 represent condensation advected upwards through cloud-base.

However, the third budget, from E3 to E4, is qual-

itatively different than the other two. The BL had become very unstable over the core of the Gulf Stream, the number of steam plumes decreased from E3 to E4, and by E4 there was precipitation. We would expect some evaporation of precipitation falling into the drier subcloud layer. The vector $A'4$ represents a *cooling* and drying of the subcloud layer and is probably a combination of a cloud base flux (which warms and dries) and the net evaporation of precipitation in the subcloud layer that cools and moistens (a large source, S), similar to the hurricane subcloud layer budget presented in Betts and Simpson (1987). We do not have profiles through cloud-base for these stacks, or measured fluxes at cloud-base, but we can show these processes schematically in Fig. 9. The light dashed vectors show how the vector $A'4$ could be the sum of a cloud-base flux (unstable to θ_e) and net subcloud evaporation of precipitation (at constant θ_e).

Our cloud-base height estimate has considerable uncertainty, and this affects the estimate of cloud-base fluxes. Because of the large air–sea temperature difference, the fluctuations of θ and q (and the corresponding values of LCL) in the subcloud layer were large. Furthermore, visual cloud-base was very uneven and often obscured by steam (Fig. 3). However, Fig. 9 shows the sum of the convective fluxes and any net condensation at other levels in the subcloud layer. For example, in the budget from E2 to E3, $A'3$ represents the fluxes at a mean height of 800 m, including condensate advected upward through that level. For a mean height of 600 m the convective fluxes needed to balance the budget are represented by AG. This is a considerable change from $A'3$, representing a much larger upward flux of θ_e.

8. Summary and discussion

In this paper we have described an aircraft exploration of air–sea interaction accompanying an extreme, cold-air outbreak from the eastern coast of the United States during the GALE. Data was obtained from NCAR's Electra aircraft on 28 January 1986. Visual observations of the meteorological conditions during the flight were highlighted by a lowering of cloud-base downstream and a subcloud layer filled with plumes of steam rising from the warm ocean surface. The steam plumes increased in number after reaching the western Gulf Stream front and began to taper off after passing over the core of the Gulf Stream; near the eastern Gulf Stream front snow showers were encountered. Above the cloud layer, aboard the NASA Electra, downward-looking lidar measurements and visual observations indicated that cloud top was increasing with fetch and that a overcast stratocumulus cloud deck had transformed into nearly overcast cumulus congestus clouds at the eastern edge of the Gulf Stream; these observations are consistent with the subcloud layer observations of snow showers and with satellite imagery (Fig. 1).

The primary difference between this situation and intense cold air advection over the adjacent continent (where surface-air temperatures can also be large initially) is the effect of the almost unlimited supply of sensible and latent heat at the ocean surface. Thus it is not surprising that the sum of latent and sensible heat fluxes measured from the aircraft are among the highest ever observed over the ocean.

In that respect we have the following hierarchy of total energy exchange from ocean to atmosphere: in the latitude belt 30°–40°N, an annual average of 70°W m^{-2}; within the same latitude belt but just off the eastern coast of the United States, an annual average of 380 W m^{-2}; for the same area, a January monthly average of 550 W m^{-2}; within a much smaller area over the Gulf Stream during a January cold air outbreak we observed a peak total flux of about 1000 W m^{-2} (see also Bane and Osgood 1989).

Assuming two cold air outbreaks a winter month, each lasting about two days, and that one-third of the area is associated with a total flux of 1000 W m^{-2} while the rest is associated with about 700 W m^{-2} (slightly less than the lowest level flux measured over the 20°C water of the eastern Gulf Stream front), then extreme cold air outbreaks could account for about 20 percent of the monthly average loss of energy from ocean to atmosphere during winter. For the remaining time, when two more moderate cold air outbreaks would probably occur, an area average sensible plus latent heat flux of about 440 W m^{-2} would be necessary to achieve Bunker's (1976) January monthly estimate of 550 W m^{-2}.

We investigated air mass transformation by evaluating the relative importance of the components of the Lagranginan budgets of potential temperature and moisture as the dry Arctic air flowed over the Gulf Stream. Lagrangian change, turbulent flux divergence, and radiative flux divergence (for the potential temperature budget) were estimated, while the sum of source and sink terms for the two budgets were evaluated as residuals of the budget.

Cross sections of potential temperature (corrected for diurnal heating of the land surface at the coast), moisture, and windspeed were constructed from the aircraft data (Fig. 2). The potential temperature cross section shows the air rapidly warming between the coast and the western Gulf Stream front with less rapid warming thereafter. This sequence is mirrored in the moisture cross section. Combining the two indicates that the air in the layer investigated was slightly unstable as it moved away from shore and became progressively more unstable over the Gulf Stream core and eastward. The cross section of horizontal windspeed showed that the windspeed increased with fetch and that a wind maximum formed *within the subcloud layer,* which

was distinct from another maximum observed near cloud top.

Estimates of Z_i/L indicate that the first three stacks were flown in a region where horizontal roll vortices may coexist with convective cells (and most likely modulate them into alongwind rows), while the last stack was flown in nearly free convective conditions where random organization of convective cells would be predominant. Thus the crosswind orientation of the first three stacks was important in obtaining good statistical confidence in flux measurements.

We adopted the convention of Chou and Zimmerman (1989) that the height of the convecting layer, Z_i, was the top of the cloud layer rather than cloud-base. Scaled in this manner, we found that vertical profiles of standard deviations of horizontal velocity, vertical velocity, temperature, and moisture were comparable to, though more intense than those measured in other studies of cold air outbreaks. In general standard deviations increased with fetch. Flux convergence of potential temperature and moisture also increased with fetch and showed indications of a decrease east of the Gulf Stream core.

Considering that the correlation coefficient (ratio of actual flux to potential flux) is a measure of flux transfer efficiency, the correlation coefficients for both potential temperature and moisture flux were very high. This indicates that very little mixing was occurring between upward and downward moving convective cells. This would suggest that the subcloud and cloud layers were highly coupled, which is consistent with the use of cloud top as Z_i.

The evaluation of the Lagrangian budgets of potential temperature and moisture was carried out by looking at each budget separately and comparing the two residuals as well as combining the budgets in a graphical representation. Budgets were evaluated between stacks E1–E2 (cold water to western Gulf Stream front) and E2–E3 (western Gulf Stream front to Gulf Stream core). The budget for E3–E4 can only be used as a rough guide because the presence of convective activity probably compromised the flux divergence estimates. We found the sensible heat budget to be sensitive to the correction for diurnal heating of the coastal land surface. Because of lack of evidence to the contrary we assumed that there was little diurnal variation in absolute humidity.

As expected, flux convergence (Table 4a; Fig. 8, and Fig. 9) accounted for the bulk of the potential temperature change between the stacks (74%–80%). Despite the very large air–sea temperature difference, the measured radiative flux divergence component accounted for only about 5 percent of the potential temperature change between both E1–E2 and E2–E3. However, a residual warming was noted that comprised about 13 percent of the average low-level aircraft sensible heat flux for stack pairs E1–E2 and E2–E3. This residual warming was also seen in the graphical representation. A drying was found in the latent heat budget corresponding to 16 and 10 percent of the stack-pair low-level latent heat flux for E1–E2 and E2–E3, respectively. *We suggest that this warming and drying is the result of heating by condensation of water vapor in the subcloud layer, which is advected upward out of the budget layer into the cloud-base.* This is consistent with visual observations of steam rising from the surface to cloud-base (see Fig. 3). Furthermore, there was probably a great deal of condensate present that was not visible to the naked eye. We hypothesize that condensation warming may be related to subcloud layer relative humidity that appeared to have diurnal variability.

Clearly there are considerable uncertainties in these budgets: in the moisture fluxes through the Lyman-alpha calibration, in the effect of the diurnal correction on the θ budget, in the net radiative heating, and in the downward and upward extrapolation of the aircraft data. However, the graphical representation presents a useful synthesis of the heat and moisture budgets. One can visually assess changes to the budgets resulting from errors in their terms. The stack budgets show residuals, generally consistent with a net condensation in the subcloud layer. The graphical subcloud layer budgets (from the ocean surface to cloud-base) between E1–E2 and E2–E3 show some combination of large fluxes through cloud-base and net condensation in the subcloud layer. This net condensation might represent as much as 55 percent of the residual. The subcloud layer budget to the east of the Gulf Stream core (from E3 to E4) was qualitatively different and suggested that the subcloud layer was being modified by the evaporation of precipitation falling into the subcloud layer as well as large cloud-base fluxes.

We emphasize the exploratory nature of this investigation. While some characteristics of cold air outbreaks have been observed previously, this is the first attempt to evaluate thermodynamic budgets in the subcloud layer associated with the airmass transformation. As mentioned before, data could only be gathered in the middle portion of the subcloud layer, which left two important layers unobserved: the layer from the surface to about 70 m and the first 100 or so meters below the lowest cloud base. Both layers are probably important to the airmass transformation process. The near surface layer is strongly superadiabatic and its potential temperature budget probably involves a large convective convergence, a large radiative flux convergence, and evaporation of spray and steam condensation. We have made estimates of the surface fluxes, but the uncertainties are considerable. Similarly, the graphical approach has suggested that the layer above the uppermost flight level may also be subject to strong flux transports through cloud-base and diabatic heat sources and sinks. Exploration of these layers are also

a challenge to future investigations of airmass transportation.

Early in the GALE Field Phase, radar, lightning, and aircraft observations confirmed the importance of convective processes in rapid cyclogenesis. We have some comments regarding the transformation of a cold-air outbreak airmass from one which would inhibit convective processes to one which would promote the observed convective processes. Based on the lifted index, boundary layer air would have to have a θ_e of about 317 K for the air to contribute to deep convection during a storm (Kreitzberg, personal communication 1989). The boundary layer air near E3, which had undergone considerable adjustment from coastal values by the addition of sensible heat and moisture, had a θ_e around 281 K. The Lagrangian time rate of change between E3–E4 of θ_e was about 1.6 K h^{-1} as the air flowed away from the Gulf Stream core to the eastern side of the Gulf Stream. Sea surface temperatures of about 22°–20°C extend for several hundred kilometers to the east of the Gulf Stream core thus continuing to support warming and moistening of the airmass flowing eastward. As a lower bound to the boundary layer recovery time we assume that the Lagrangian change from E3–E4 was representative of the change to the east of the Gulf Stream. Using this time change it would take roughly 19 hours for the air to reach a θ_e value around 317 K. As the air warmed and moistened and the sea–air temperature difference decreased, it is reasonable to assume that the turbulent flux convergence would decrease. Betts and Ridgway (1989) show a boundary layer equilibrium $\theta_e \approx 319$ K over a sea surface temperature of 20°C. We conclude that the boundary layer recovery time to support deep convection is on the order of 20–30 hours. During rapid cyclogenesis, warm, moist boundary layer air is necessary and observations during the field phase indicated that it could be advected from the south and southeast; however, it is also possible that in the interval between synoptic forcings, boundary layer air following a cold air outbreak has had time to gain enough moist static energy to participate in cyclogenesis.

Finally, we wish to point out the diurnal character of coastal airmass modification during cold air outbreaks. This modification is dependent upon land surface processes that have considerable diurnal variability during the clear sky conditions associated with a cold air outbreak as well as ocean surface processes that have little diurnal variation. Daytime heating of the land would warm and possibly dry subcloud-layer air while at night radiational cooling would cool the air leaving the coastal land area. These widely varying initial conditions would most likely affect the rate that the warmer ocean surface would warm and moisten the air flowing over it.

The budgets we have presented are a *snapshot of the air–sea interaction processes* leading to airmass transformation during a cold air outbreak, taken about midmorning of the diurnal heating cycle over land. Airmass heating over land during the warming phase of the diurnal cycle was about 55 percent of the sensible heating observed from stack E1–E4 (6.5 C versus 11.0 C). Thus the time it takes to precondition boundary layer air so that it contains enough convective available potential energy to participate in deep convective processes is probably dependent upon the time of day the cold air outbreak began.

Acknowledgments. This paper is dedicated to the late Andrew Bunker of Woods Hole Oceanographic Institution who was fascinated by the beauty and physics of cold air outbreaks; his ideas contributed to fundamental progress in understanding the physics of the marine boundary layer. The participation of NCAR's Research Aviation Facility in GALE was invaluable. NCAR is sponsored by the National Science Foundation. NCAR Pilot Henry Boynton, co-pilot Gil Summers, the Electra crew, and student observers are gratefully thanked for a job well done under difficult conditions. Robert L. Grossman (RLG) was the GALE Mission scientist responsible for planning and executing the Electra mission. Computations relating to this paper were carried out thanks to a grant of computer resources from the Scientific Computing Division of NCAR whose consultants and staff supplied valuable help. Thanks also to Drs. Harvey Melfi and Reinout Boers in the NASA Electra for excellent coordination with the NCAR Electra during the joint mission. The photo used for Fig. 3 was taken by student observer Nancy Lang. We benefited from discussions with Drs. Shu-Hsien Chou, John Bane, Tom Ackerman, and Greg Holland and from thoughtful reviews by Drs. Boers and Chou. RLG is particularly indebted to Dr. Chou for discussions about the Lyman-alpha calibration method. RLG was supported by the National Science Foundation Grant ATM-8518972 and by NASA Goddard Space Flight Center Contract NAS5-29366. Allan K. Betts was supported by the National Science Foundation Grant ATM87-05403 and by NASA Goddard Space Flight Center Contract NAS5-30524.

REFERENCES

Augstein, E., 1979: The atmospheric boundary layer over the tropical oceans. *Meteorology Over the Tropical Oceans,* D. B. Shaw, Ed., Royal Meteorological Society, 73–103.

Bane, John M., and Kenric E. Osgood, 1989: Wintertime air–sea interaction processes across the Gulf Stream. *J. Geophy. Res. (Oceans)* **94,** 10 755–10 772.

Bean, B. R., R. Gilmer, R. L. Grossman, R. McGavin and C. Travis, 1972: An analysis of airborne measurements of vertical water vapor flux during BOMEX. *J. Atmos. Sci.,* **26,** 860–869.

Betts, A. K., 1984: Boundary layer thermodynamics of a High Plains severe storm. *Mon. Wea.Rev.,* **112,** 2199–2211.

——, and J. Simpson, 1987: Thermodynamic budget diagrams for the hurricane subcloud layer. *J. Atmos. Sci.,* **44,** 842–849.

——, and W. Ridgway, 1989: Climatic equilibrium of an atmospheric

convective boundary layer over a tropical ocean. *J. Atmos. Sci.*, **46,** 2621–2641.

Boers, R., and A. K. Betts, 1988: Saturation point structure of marine stratocumulus clouds. *J. Atmos. Sci.* **45,** 1157–1175.

Budyko, M. I., 1963: Atlas of heat balance of the Earth's surface. USSR Glavnaia Geofizicheskaia Observatoriia, Moscow, 69 pp. [See also Guide to the Atlas of the heat balance of the Earth, I. A. Donehoo (translator), US Weather Bureau, WB/T106, Washington, D.C., 25 pp.]

Bunker, A. F., 1960: Heat and water vapor fluxes in air flowing southward over the western North Atlantic Ocean. *J. Meteor.*, **17,** 52–63.

——, 1976: Computations of surface energy flux and annual air–sea cycles of the North Atlantic Ocean. *Mon. Wea. Rev.*, **104,** 1122–1139.

——, and L. V. Worthington, 1976: Energy exchange charts of the North Atlantic Ocean. *Bull. Amer. Meteor. Soc.*, **57,** 450–467.

Chou, S.-H., D. Atlas and E.-N. Yeh, 1986: Turbulence in a convective marine atmospheric boundary layer. *J. Atmos. Sci.*, **43,** 547–564.

——, and J. Zimmerman, 1989: Bivariate conditional sampling of buoyancy flux during an intense cold air outbreak. *Bound.-Layer Meteor.*, **46,** 93–112.

Dirks, R. A., J. P. Kuettner and J. A. Moore, 1988: Genesis of Atlantic Lows Experiment (GALE): an overview. *Bull. Amer. Meteor. Soc.*, **69,** 148–172.

Dunckel, M., L. Hasse, L. Krugermeyer, D. Schriever and J. Wunknitz, 1974: Turbulent fluxes of momentum, heat, and water vapor in the atmospheric surface layer at sea during ATEX. *Bound.-Layer Meteor.*, **6,** 81–106.

Fairall, C. W., J. B. Edson and M. A. Miller, 1989: Heat fluxes, whitecaps, and seaspray. *Surface Waves and Fluxes: Current Theory and Remote Sensing,* G. Greenaert and W. Plant, Eds., Kluwer Press, 830 pp.

Friehe, C. A., R. L. Grossman and Y. Pann, 1986: Calibration of an airborne Lyman-alpha hygrometer and measurement of water vapor flux using a thermoelectric hygrometer. *J. Atmos. Ocean. Tech.*, **3,** 299–304.

Greenaert, G. L., K. Katsaros and K. Richter, 1986: Variation of the drag coefficient and its dependence upon sea state. *J. Geophys. Res.*, **91,** 7667–7679.

Grossman, R. L., 1982: An analysis of vertical velocity spectra obtained in the BOMEX fair-weather trade-wind boundary layer. *Bound.-Layer Meteor.*, **23,** 323–357.

——, and D. R. Durran, 1984: Interaction of low-level flow with the western Ghat mountains and offshore convection in the summer monsoon. *Mon. Wea. Rev.*, **112,** 652–672.

——, 1984: Bivariate conditional sampling of moisture flux over a tropical ocean. *J. Atmos. Sci.*, **41,** 3238–3253.

——, and C. A. Friehe, 1986: Vertical structure of the southwest monsoon low-level jet over the central and eastern Arabian Sea. *J. Atmos. Sci.*, **43,** 3266–3272.

——, and S.-H. Chou, 1989: Comments on "Calibration of an airborne Lyman-Alpha hygrometer and measurement of water vapor flux using a thermoelectric hygrometer": effect of low-pass filtering. Submitted to *J. Atmos. Oceanic Technol.*

Konrad, C. E., II, and S. J. Colucci, 1989: An examination of extreme cold air outbreaks over eastern North America. *Mon. Wea. Rev.*, **117,** 2687–2700.

Konrad, T. G., 1970: The dynamics of the convective process in clear air as seen by radar. *J. Atmos. Sci.*, **27,** 1138–1147.

Kuettner, J., 1959: The band structure of the atmosphere. *Tellus,* **11,** 267–294.

LeMone, M. A., 1973: The structure and dynamics of horizontal roll vortices in the planetary boundary layer. *J. Atmos. Sci.*, **30,** 1077–1091.

Lenschow, D. H., 1974: Model of the height variation of the turbulence kinetic energy budget in the unstable planetary boundary layer. *J. Atmos. Sci.*, **31,** 465–474.

——, J. C. Wyngaard and W. T. Pennell, 1980: Mean-field and second-moment budgets in a baroclinic, convective boundary layer. *J. Atmos. Sci.*, **37,** 1313–1326.

Long, B., and H. P. Hanson, 1985: Climatology of cyclogenesis over the east China Sea. *Mon. Wea. Rev.*, **113,** 697–707.

Mercer, T. J., and C. W. Krietzberg, 1986: Genesis of Atlantic Lows Experiment (GALE) Field Program Summary. [Available from GALE Data Center, Dept. Physics and Atmos. Sci., Drexel University, Philadelphia, PA 19104.] 152 pp.

Miller, E. R., and R. B. Friesen, 1985: Standard Output Data Products from the NCAR Research Aviation Facility. NCAR Research Aviation Facility Bulletin No. 9. [Available from NCAR, POB 3000, Boulder, CO 80307.]

Ninomiya, K., 1973: Variation in the heat energy budget over the East China Sea associated with the passage of wave cyclones in February 1968. *J. Meteor. Soc. Japan,* **51,** 435–449.

——, and T. Akiyama, 1976: Structure and heat energy budget of mixed layer capped by inversion during the period of polar outbreak over Kuroshio region. *J. Meteor. Soc. Japan,* **54,** 160–174.

Palm, S. P., S. H. Melfi and R. Boers, 1988: Genesis of Atlantic Lows Experiment: NASA Electra Boundary Layer Flights Data Report. NASA Tech. Memo. 100703, NASA Management Information Division, Washington, DC 20546-0001. 210 pp.

Palmen, E., and C. W. Newton, 1969: *Atmospheric Circulation Systems: Their Structure and Physical Interpretation.* Academic Press, 603 pp.

Riehl, H., 1979: *Climate and Weather in the Tropics.* Academic Press, 611 pp.

——, T. C. Yeh, J. S. Malkus and N. E. LaSuer, 1951: The northeast trade of the Pacific Ocean. *Quart. J. Roy. Meteor. Soc.*, 77, 598–626.

Sheppard, P. A., and M. H. Omar, 1952: The wind stress over the ocean from observations in the trades. *Quart. J. Roy. Meteor. Soc.*, **78,** 583–589.

——, D. T. Tribble and J. R. Garratt, 1972: Studies of turbulence in the surface layer over water (Lough Neagh). Part I: Instrumentation, programme, profiles. *Quart. J. Roy. Meteor. Soc.*, **98,** 627–641.

Uccellini, L. W., K. F. Brill, R. A. Petersen, D. Keyser, R. Aune, P. J. Kocin and M. des Jardins, 1986: A report on the upper-level wind conditions preceding and during the shuttle *Challenger* (STS 51L) explosion. *Bull. Amer. Meteor. Soc.*, **67,** 1248–1265.

WMO, 1981: Scientific results of the Air Mass Transformation Experiment (AMTEX). GARP Publ. Ser., 24, 236 pp.

Webb, E. K., G. I. Pearman and R. Leuning, 1980: Correction of flux measurements for density effects due to heat and water vapour transfer. *Quart. J. Roy. Meteor. Soc.*, **106,** 85–100.

Woodcock, A. H., 1940: Convection and soaring over the open sea. Sears Foundation. *J. Mar. Res.*, **3,** 248–253.

Zipser, E. J., and M. A. LeMone, 1980: Cumulonimbus vertical velocity events in GATE. Part II: Synthesis and model core structure. *J. Atmos. Sci.*, **37,** 2458–2469.